AIAA 81-0160R

Numerical Simulations of a Segmented-Plenum, Perforated, Adaptive-Wall Wind Tunnel

J. C. Erickson Jr.* and G. F. Homicz†
Aerodynamic Research Department, Calspan Advanced Technology Center, Buffalo, N.Y.

Flow within the tunnel is simulated by modeling the incompressible interaction of the transpired turbulent boundary layers on the walls with the flow over the airfoil. Despite the fact that a finite number of plenum chambers can exert only imperfect control over the flow, it is demonstrated that one can still achieve what is for all practical purposes unconfined flow about the airfoil. Velocity differences produced at control surfaces outside the boundary layers by changing the pressure in one plenum chamber at a time, holding the other chamber pressures constant, are presented as influence functions. Implications of the analysis on tunnel design and automation are described.

Nomenclature

c_f, c_{f0} = friction coefficients with and without transpiration, respectively
c_p = pressure coefficient on airfoil surface, $(p-p_\infty)/q_\infty$
c_{pn} = pressure coefficient in plenum n, $(p_e-p_n)/q_\infty$, Eq. (2)
c = airfoil chord, Fig. 1
H = boundary-layer shape factor, δ^*/θ
h = distance from model to tunnel walls, Fig. 1
I_u, I_v = influence functions for u and v determined from simulations, defined in Eqs. (5) and (6)
$\hat{I}_u, \hat{I}_v$ = idealized influence functions, defined in Eqs. (B17) and (B18)
l_n = length of plenum chamber n
M = Mach number
p = static pressure
q = dynamic pressure
U = total velocity component in x direction
u,v = perturbation velocity components in x, y directions
$\Delta u, \Delta v$ = change in u, v after pressure in one plenum is changed
δu = $\Delta u(\infty) - \Delta u(-\infty)$
v_e = effective inviscid normal velocity at wall due to boundary-layer displacement (positive out of the wall), Eq. (4)
v_w = transpiration velocity at wall (positive out of the wall)
x,y = coordinate system with origin at airfoil quarter chord, Fig. 1
x_n = streamwise location of center of plenum chamber n
$\bar{x}$ = $(x-x_n)/l_n$
y_c = distance from tunnel centerline to control surfaces, Fig. 1
$\bar{y}$ = y/h
α = airfoil angle of attack
β = $(1-M_\infty^2)^{1/2}$
δ = boundary-layer thickness
δ^* = boundary-layer displacement thickness
θ = boundary-layer momentum thickness
ξ,η = coordinate system with origin at the center of plenum chamber n midway between the walls
ϕ = disturbance velocity potential in Appendix B

Subscripts

a = evaluated at control surface adjacent to plenum chamber n
e = condition at edge of boundary layer
n = condition in plenum n
o = evaluated at control surface opposite to plenum chamber n
∞ = freestream condition

I. Introduction

THE concept of an adaptive-wall wind tunnel has attracted much attention recently[1-14] because of its promise for significant reductions in tunnel-wall interference, particularly in the transonic flight regime. An adaptive-wall wind tunnel[1-3] provides for active control of the flow in the vicinity of test-section walls in order to minimize or eliminate interference on the model. The distributions of the disturbance velocity components are measured at discrete points along control surfaces, or interfaces, in the flowfield near the walls, but away from the model and outside the boundary layers on the walls. A theoretical representation for the flow exterior to these control surfaces, including the desired unconfined-flow boundary condition that all disturbances vanish at infinity, is used to establish the functional relationships that must be satisfied at the control surfaces by the measured disturbance velocities. If the measured velocities do not satisfy these relationships, an iterative procedure provides a new approximation for the flowfield at the surfaces, and the wall control is readjusted until the measured quantities satisfy the functional relationships for unconfined flow.

Although the ultimate application is to fully three-dimensional flows, most of the adaptive-wall work to date has been carried out in two dimensions. Several different adaptive-wall implementations have been investigated experimentally in two dimensions, namely: impermeable, flexible walls,[9-11] perforated walls with constant plenum pressure but a porosity distribution that varies in the streamwise direction,[12] perforated walls with constant plenum pressure and a porosity that is uniform along each wall but can vary from one wall to another[12] (including a

Presented as Paper 81-0160 at the AIAA 19th Aerospace Sciences Meeting, St. Louis, Mo., Jan. 12-15, 1981; submitted Feb. 20, 1981; revision received Oct. 6, 1981.

*Principal Engineer; now Senior Research Engineer, Propulsion Wind Tunnel Facility, Calspan Field Services, Inc., AEDC Division, Arnold Air Force Station, Tenn. Member AIAA.
†Principal Engineer. Member AIAA.

three-dimensional application[13]), slotted walls with segmented plenum chambers,[14] and perforated walls with segmented plenum chambers.[2-8] In the latter two ventilated-wall implementations, the pressure in each of the approximately 20 segmented plenum chambers can be controlled individually.

Simulations of adaptive-wall tunnels, including theoretical representations of the flow within the tunnel, played an important role in the early development of the concept. Simulations were carried out by several investigators for incompressible flows,[4,15] compressible, subcritical flows,[16-19] and flows that are supercritical at the tunnel walls.[4,17,18] Not only did these studies demonstrate numerically that the overall procedure converged to unconfined flow, even for supercritical walls, but they also cast a great deal of light on the nature of the iterative process, especially the necessity for underrelaxation of the iterations. Furthermore, the accuracy required in satisfaction of the functional relationships for unconfined flow was examined. These simulations were highly idealized, however. No attempt was made to model the flow in the vicinity of actual wall configurations. Instead, it was assumed that perfect control of either the streamwise, u, or normal, v, disturbance velocity component was available everywhere along the control surfaces, even at shock waves. The only exception was a study by Sears,[19] who considered an approximate representation of imperfect wall control and examined the errors in the converged solutions.

A two-dimensional perforated-wall, segmented-plenum configuration has been investigated extensively at Calspan in the One-Foot Wind Tunnel, and the experimental configuration has been described previously.[2-8] It is not absolutely necessary to know the details of the flow in the vicinity of the walls in order to achieve unconfined-flow conditions. That is, if the desired disturbance velocities at the control surfaces can be set experimentally at each step of the iterative procedure, the details of the flow at the walls are of little interest. As the experimental investigation proceeded,[2-8] however, it was concluded that operational procedures for exercising wall control, including its eventual automation, could be enhanced by development of more realistic simulations. These simulations would model the flow through the walls, the influence of that flow on the wall boundary layers, and, consequently, the interaction with the flow within the control surfaces.

The simulation methodology developed for two-dimensional incompressible flows is described in Sec. II, and some details are given in Appendix A. Results for the incompressible-flow approximation should be representative of subsonic, subcritical flows in general. Results for the baseline simulation of a 6% blockage NACA 0012 airfoil section at an angle of attack α of 4 deg are presented in Sec. III. Influence functions for the velocity perturbations introduced in the test section by changing the pressure in one plenum chamber at a time, while holding the pressure in the other chambers constant, are presented in Sec. IV and are compared with idealized influence functions that are derived in Appendix B. Finally, major conclusions drawn from the simulations are presented.

II. Methodology

Tunnel Configuration

The Calspan 0.305-Meter (One-Foot) Wind Tunnel[3,4] is a continuous-flow, closed-circuit facility that operates at Mach numbers from about 0.5 to 0.95 at a unit Reynolds number of 6.56×10^6 per meter (2×10^6 per foot). The adaptive-wall test section is two-dimensional, with perforated top and bottom walls of 22.5% open-area ratio. The plenum chambers behind the perforated walls have been divided into 18 segments, 10 on the top and 8 on the bottom, and each segment is connected to a pressure and a suction source through individual control valves. The pressure source is the tunnel stilling chamber, and the suction source is an auxiliary compressor discharging into the tunnel circuit in the diffuser.

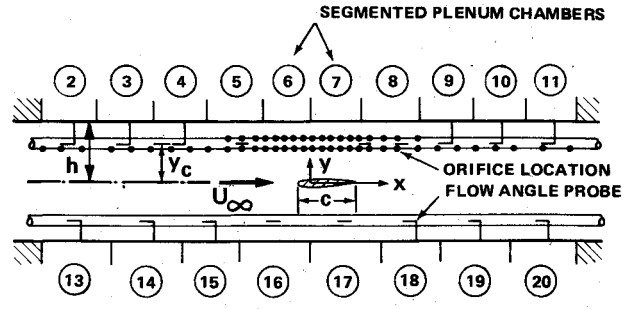

Fig. 1 Schematic of Calspan One-Foot Adaptive-Wall Wind Tunnel.

The model and test section are shown schematically in Fig. 1. The model is an NACA 0012 airfoil section with a 0.152-m (6.0 in.) chord c (6% solid blockage) and is situated midway between walls that are located at $y = \pm h = \pm 0.152$ m (± 6.0 in.). The test-section instrumentation at the control surfaces consists of flow-angle probes and static-pressure pipes. The control surfaces are located outside the wall boundary layers at $y_c = \pm 0.100$ m (± 3.93 in.). The u and v disturbance velocity components are determined from measurements made with this instrumentation.[7]

The simulation procedure that is developed here does not provide directly for simulation of the iterative process used in running the Calspan tunnel. That is, it does not simulate the plenum-pressure adjustment technique that is used[3,4] to set desired $u(x, \pm y_c)$ distributions in the tunnel. Such simulations could be developed later, if desired, on the basis of the model described here.

Calculation Method

Simulation of the flow within this adaptive-wall test section requires solutions for the flow over the airfoil in the presence of the viscous effects at the perforated, segmented, plenum-pressure-controlled walls. Outside the wall boundary layers, the flow is assumed to be inviscid. For the inviscid flow, a procedure is required for calculating the flow over a model with prescribed distributions of the normal velocity components as boundary conditions at the walls. Two tools are needed to treat the wall boundary layers. First, a relationship is required between the transpiration velocity at the wall and the pressure drop across the wall. Second, a method is needed for calculating the characteristics of turbulent boundary layers with a transpiration velocity (either into or out of the walls) that is continuous over each plenum segment but is likely to be discontinuous at junctions between segments.

Inviscid-Flow Model

A computer program developed originally to predict the two-dimensional flow over airfoils in a solid-wall wind tunnel with nonuniformly sheared freestreams[20,21] had been modified[15] to simulate the inviscid flow within an adaptive-wall wind tunnel and was adapted further for this investigation. The computer program can accommodate airfoils with arbitrary thickness and camber. In the program, the airfoil is represented by a vortex distribution along its actual surface and the walls are represented by surface source distributions. These vortex and source distributions are broken up into small segments, each of which has a constant strength. Beyond a specified distance from the airfoil, both upstream and downstream, the source distributions at the walls are assumed to decay inversely with x as x approaches $\pm\infty$ because the source strength is closely related to the normal velocity there. The velocity components induced at any field point by each segment are given by closed-form algebraic expressions. Total velocity components due to the walls and the airfoil are then found by summing the con-

tributions of all segments. The strength of each small segment is found by satisfying simultaneously the normal-flow boundary conditions $v(x, \pm h)$ at the walls and the condition of no normal flow through the airfoil surface. The normal-flow boundary conditions are applied at the center of each segment. For N vortex and source segments, N algebraic equations result from the boundary conditions, but only $N-1$ of them are linearly independent, as shown by von Mises.[22] Addition of the Kutta-Joukowski condition completes the set of equations, which is solved using a smoothing technique.[23,24]

Transpired-Wall Characteristics

The relationship between the transpiration velocity at the wall v_w (taken as positive out of the wall) and the pressure drop across the wall was determined empirically. Data had been obtained by Chew[25] for the same 22.5% open-area ratio walls, namely, 0.0016-m (1/16-in.)-thick plate with 0.0016-m-diam holes on 0.0032-m (1/8-in.) centers. These data, which are only for suction, were measured at Mach numbers from 0.75 to 1.175. Although these data were an averaged v_w over a long run of plate with constant plenum pressure p_n and uniform pressure p_e in the test section, it was assumed that they could be applied in the present analysis on a point-by-point basis. The data of Ref. 25 are correlated reasonably well by

$$(p_e - p_n)/M_\infty q_\infty = 0.005 + 220.0(v_w/U_\infty)^2 \qquad (1)$$

where q_∞ and M_∞ are the freestream dynamic pressure and Mach number. This result had to be extended to lower values of M_∞ and to include blowing. For blowing, Fig. 6.2 of Ref. 26 indicates that the data could reasonably be assumed to be antisymmetric about $v_w = 0$. Reference 26 also indicates that, at lower Mach numbers, Prandtl-Glauert behavior is expected. Therefore, a Prandtl-Glauert scaling was matched to the empirical variation of Eq. (1) and the antisymmetric character was accounted for to obtain

$$c_{p_n} \equiv \frac{p_e - p_n}{q_\infty} = f(M)\left[0.005 - 220.0\left|\frac{v_w}{U_\infty}\right|\left(\frac{v_w}{U_\infty}\right)\right] \qquad (2)$$

where

$$f(M) = \begin{cases} 0.5(1-M^2)^{-1/2}, & M \le (2)^{-1/2} \\ M, & M \ge (2)^{-1/2} \end{cases} \qquad (3)$$

For the incompressible-flow calculations of this study, $f(M) = 0.5$ was used.

Boundary-Layer Model

The most important characteristic of the boundary layer for the present application is its interaction with the inviscid flow. Lighthill[27] has described several ways of interpreting the displacement thickness and its effect on the inviscid flow. The interpretation chosen here is an extension to transpired walls of what Lighthill calls the method of "equivalent sources." In this procedure, the original wall surface is retained and the effect of the boundary layer on the inviscid flow is represented by a distribution of sources on this surface. This procedure has been used with success in calculations of the effect of the boundary layer on the flow over airfoils by several authors, as in Refs. 28 and 29, for example. In the present analysis then, the effect of the boundary layer on the inviscid flow is written as an inviscid velocity distribution $v_e(x)$ (taken as positive out of the wall) that, when applied at the actual wall surface, gives the proper displacement effect. For transpired boundary layers, v_e is given by

$$v_e(x) = v_w(x) + \mathrm{d}[U_e(x)\delta^*(x)]/\mathrm{d}x \qquad (4)$$

where δ^* is the boundary-layer displacement thickness, and U_e is the total inviscid streamwise velocity component outside the boundary layer. In general, $\delta^*(x)$ in Eq. (4) depends on $v_w(x)$, $U_e(x)$ and the initial conditions for the boundary-layer calculation.

Since the details of the boundary-layer profile are of less concern for this application, Head's well-known integral method[30] was adopted for the boundary-layer calculations. An outline of the method and representative results are given in Appendix A. The resulting boundary-layer equations can be integrated for arbitrarily prescribed distributions of $U_e(x)$ and $v_w(x)$ and appropriate initial conditions.

Simulation Logic

The establishment of the inviscid-flow calculation method, the wall-characteristic model, and the boundary-layer calculation method thus set the stage for development of a simulation procedure for approximating unconfined flow in the tunnel while accounting for the perforated walls with segmented-plenum chambers. First, however, ideal point-by-point wall control was examined from the standpoint of transpired turbulent boundary-layer behavior.

Both ideal and segmented-plenum wall control simulations require use of the inviscid-flow program to calculate the unconfined flow about the model at a given angle of attack. This provides the unconfined-flow distributions $u(x, \pm h)$ and $v(x, \pm h)$ at the walls so that $U_e(x) = U_\infty + u(x, \pm h)$ and hence $p_e(x)$ at each wall are known.

Ideal Wall Control

Investigations of ideal wall control were performed first in order to shed light on how the wall boundary-layer and transpiration velocity characteristics must interact to provide perfect point-by-point control of the flow within the tunnel. Calculations with this procedure then serve as guidelines for simulations of the imperfect wall control that exists in the segmented-plenum configuration.

The unconfined-flow distributions $u(x, \pm h)$ and $v(x, \pm h)$ at the walls, in the form of $U_e(x)$ and $v_e(x)$, are specified on a point-by-point basis in order to calculate the ideal, continuous wall transpiration velocity distribution $v_w(x)$, which would reproduce exactly the unconfined flow. The boundary-layer problem posed by this ideal wall control is an inverse one because U_e and v_e are prescribed and v_w must be found. Because of the implicit nature of their dependence on v_w, the governing equations cannot be integrated directly in this case, and an iterative solution becomes necessary. This is carried out at each step of the integration as follows. A value of v_w constant over the length of the step is assumed, and the equations are integrated for the step. Equation (4) is evaluated next to determine the calculated v_e, which is compared with the desired value. If they do not agree to a specified accuracy, the value of v_w is readjusted and the process is repeated iteratively until the calculated v_e agrees with the prescribed value. The $v_w(x)$ distributions that result from this calculation provide a useful reference for beginning more realistic segmented-plenum calculations, as shown next.

Segmented-Plenum Wall Control

The modeling of segmented-plenum wall control also relies on the unconfined-flow distributions $p_e(x)$ and $v_e(x)$. The heart of the procedure is then determination of p_n, the pressure in the nth plenum chamber. This is accomplished iteratively as follows. At the center of each plenum chamber, x_n, the inviscid-flow pressure $p_e(x_n)$ is known, and since an initial estimate for $v_w(x_n)$ can be obtained from the ideal-wall calculation, an initial guess for p_n can be found from Eqs. (2) and (3). With p_n and $p_e(x)$ then known, the corresponding initial approximation to $v_w(x)$ is found over the length of each plenum chamber by Eqs. (2) and (3). In general, this procedure leads to discontinuities in $v_w(x)$ at the boundaries between plenum chambers. The boundary-layer

calculation is then made over each plenum chamber in turn on the basis of the prescribed input $p_e(x)$, $v_w(x)$, and the initial conditions. The effective inviscid velocity distribution at the walls, $v_e(x)$, is found from the computed results and Eq. (4). The integral of $v_e(x)$ over each plenum chamber is then compared with the integral of the unconfined-flow distribution $v(x, \pm h)$ over the same plenum. [It should be noted that, in the different coordinate systems used for the inviscid-flow and boundary-layer calculations, $v(x,h) = -v_e(x)$ and $v(x,-h) = v_e(x)$.] The p_n are then revised and the boundary-layer calculation is repeated until the integrals of $v_e(x)$ and $v(x, \pm h)$ over each plenum agree. Satisfaction of this condition, locally at each plenum, ensures that the integral of the source elements over each wall is zero, as is the case for fully unconfined flow. This is equivalent to the fact that the drag on the airfoil is zero in unconfined, inviscid flow.

Once the $v_e(x)$ distributions at both walls have been found in this way, they are used as boundary conditions in the inviscid-flow program to calculate the flow over the airfoil in the presence of the segmented-plenum, perforated-wall constraints. Results found by such a procedure can be used to investigate the magnitude of the errors introduced by having segmented-plenum, imperfect wall control instead of ideal, perfect wall control; this is discussed in the next section.

III. Baseline Simulation Results

The example chosen for baseline simulation is the NACA 0012 airfoil of the experiments at an angle of attack α of 4 deg. This choice gives a good balance between the lift and thickness effects on the disturbance velocity field at the control surfaces and walls. Wall and control-surface locations at 1.0 and 0.655 chords above and below the model correspond to the experimental configuration. Both ideal and segmented-plenum wall control were examined for this geometry.

For ideal wall control, the calculated distribution of $v_w(x)$ and the prescribed, unconfined-flow distribution $v_e(x)$ are presented in Fig. 2 for the upper wall. Note that upstream of the origin there is suction and a favorable pressure gradient so $v_e(x)$ follows $v_w(x)$ closely. Downstream of the origin there is blowing and an adverse pressure gradient, which give rise to a ratio of v_e to v_w of 2 or greater, i.e., an amplification of the wall velocity when blowing is present. Such behavior is typical, and the reasons for it are described at greater length in Appendix A.

The results of Fig. 2 were used to initiate the iterative calculation of the streamwise distributions of $v_w(x)$ for the segmented-plenum model, as described in Sec. II. The result for the upper wall is shown as the solid curve in Fig. 3; results for the lower wall display similar behavior. The tick marks on the abscissa of Fig. 3 correspond to the junctions between plenum chambers as shown in Fig. 1. For comparison, the ideal point-by-point distribution of $v_w(x)$ from Fig. 2 is shown as the dashed curve in Fig. 3. The additional curves and data points in this and the next few figures will be discussed in Sec. IV. The streamwise distributions of $v_w(x)$ that result from the matching procedure have very large variations over each plenum chamber, with discontinuities at the junctions between plenum chambers.

The discontinuous $v_w(x)$ distributions yield correspondingly large variations in $v_e(x)$ from the boundary-layer calculations, particularly as amplified when blowing is present. The distribution of $v_e(x)$ for the upper wall is given as the solid curve in Fig. 4, along with the dashed curve, which is the unconfined-flow distribution $v(x,h)$ from Fig. 2. The large variations in $v_e(x)$ and the associated discontinuities at the plenum junctions are certainly not realistic physically. The response of the boundary layers at the junctions would not have such an extreme character. Nevertheless, these details do not have a significant influence on the resultant flow conditions at the control surfaces or model, as will be seen below, so this representation was retained.

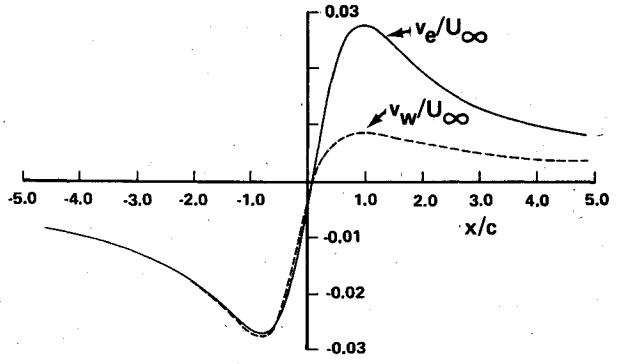

Fig. 2 Comparison of distributions of prescribed inviscid normal velocity v_e/U_∞ and calculated wall velocity v_w/U_∞ for ideal wall control (upper tunnel wall at $y/c = 1.0$).

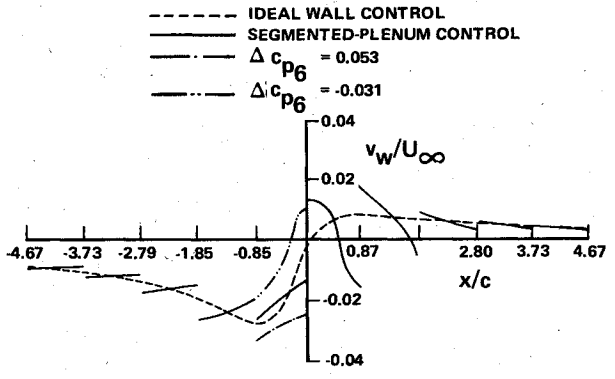

Fig. 3 Transpiration velocity at upper tunnel wall, $y/c = 1.0$, for segmented-plenum control.

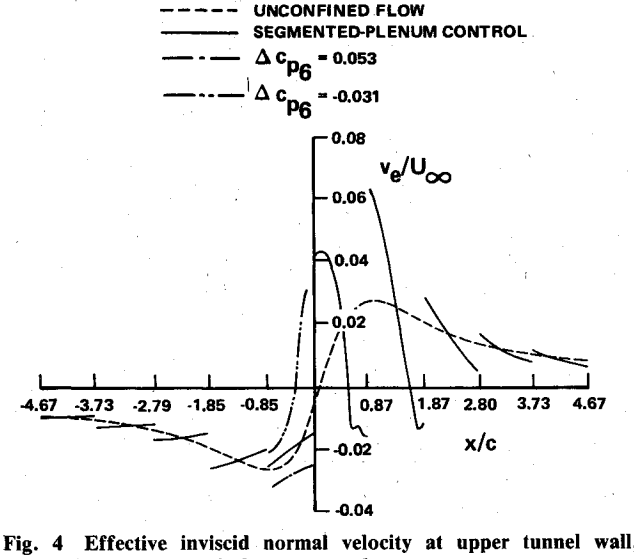

Fig. 4 Effective inviscid normal velocity at upper tunnel wall, $y/c = 1.0$, for segmented-plenum control.

The segmented-plenum $v_e(x)$ distribution of Fig. 4, and its counterpart at the lower wall, were used as boundary conditions in the calculation of the inviscid flow about the airfoil. Results for the streamwise and normal velocity components at the upper and lower control surfaces are presented in Figs. 5 and 6 by the crosses. The unconfined-flow distributions are given by the dashed curve, and the results given by the circles will be discussed in Sec. IV.

Examination of Figs. 5 and 6 indicates that agreement between the segmented-plenum and unconfined-flow distributions is generally excellent where suction is present at the walls, namely, upstream of the origin at the upper control

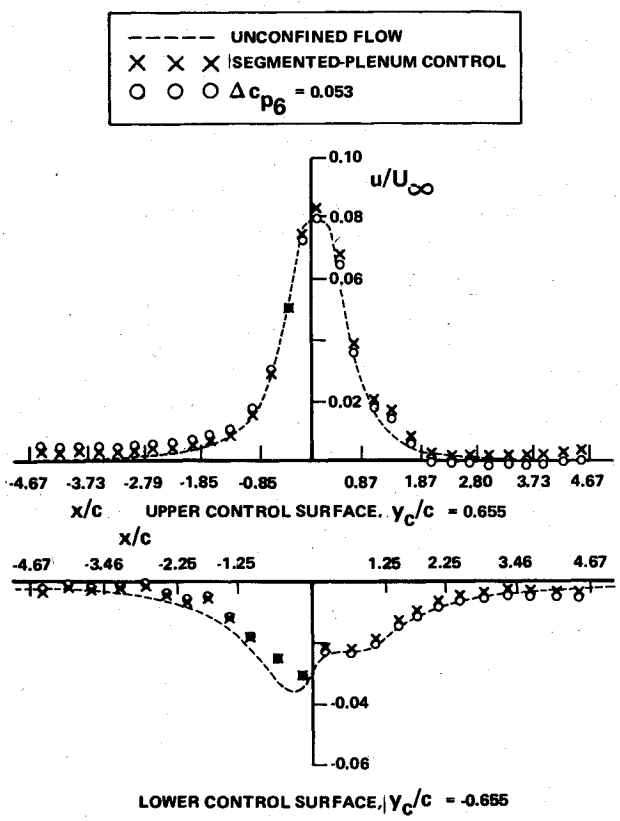

Fig. 5 Comparison of streamwise disturbance velocity at control surfaces for unconfined flow and segmented-plenum control.

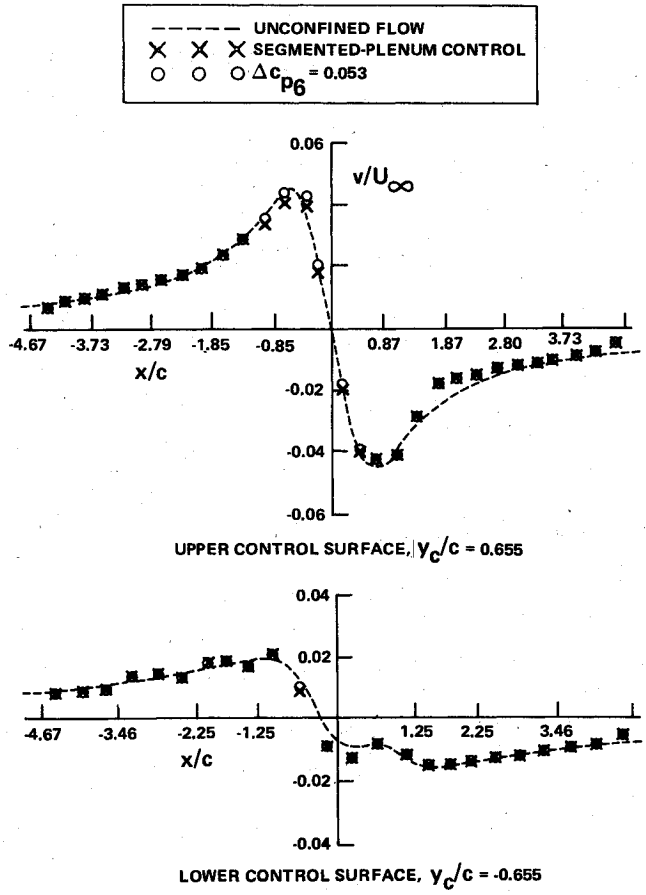

Fig. 6 Comparison of normal velocity at control surfaces for unconfined flow and segmented-plenum control.

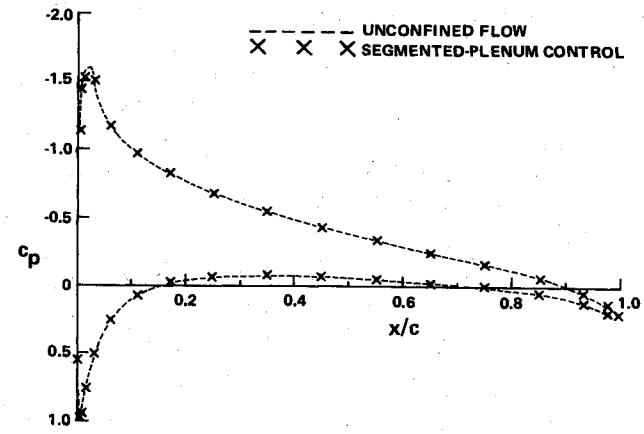

Fig. 7 Comparison of airfoil pressure distributions for unconfined flow and segmented-plenum control.

surface and downstream of the origin at the lower control surface. The discrepancies observed in u at the upstream and downstream limits of the test section result from truncation of $v_e(x)$ from the distributions shown in Fig. 4 to zero upstream and downstream of the controlled part of the test-section walls. Repeating the inviscid-flow calculations with $v_e(x)$ equal to the unconfined-flow distributions beyond the controlled sections resulted in excellent agreement of u at the upstream and downstream limits of the test section.

Overall, the results indicate that the finite size of the plenum chambers and the attendant large variations in $v_e(x)$ from modeling the flow at the walls do not prevent the realization of a good approximation to the unconfined-flow distributions for these low-speed flow conditions. This is consistent with the earlier experimental demonstrations of the adaptive-wall concept for flows that are supercritical at the model but subcritical at the control surfaces and walls.[3,4] In those cases, the desired flows could be set up experimentally without large fluctuations in the measured streamwise velocity components from point to point.

The distributions of the pressure coefficient c_p on the airfoil surface are given in Fig. 7, with the dashed lines indicating unconfined flow and the crosses the results of the segmented-plenum model. The excellent agreement shown is confirmed by integrating the c_p distributions to obtain normal force coefficients of 0.490 for unconfined flow and 0.482 for the segmented-plenum model, a difference of only 1.6%. The remarkable agreement in both the airfoil c_p distributions and the disturbance velocity distributions at the control surfaces, despite the unrealistic nature of the $v_e(x)$ distributions, results from the elliptic nature of the governing equations of motion for the flow within the tunnel.

We believe that these simulations, despite the exaggerated variations of $v_w(x)$ and $v_e(x)$ over the individual plenum chambers, especially at the plenum junctions, model the essential features of the flow near the walls. We believe further that the qualitative features of these baseline simulations, although they are strictly for incompressible flow, can be generalized to compressible, subcritical flow because there are no fundamental differences in the flow phenomena involved. If the flow were supercritical at the walls, however, different phenomena would arise and modeling of the shock-wave/boundary-layer interaction would be necessary.

The existing simulation methodology can serve as the basis for further investigations of the behavior of adaptive-wall wind tunnels with this wall configuration. It can be used to examine the effects of plenum chamber number and size and of the porosity distribution of the perforated walls. Also, it forms a framework for development of more systematic procedures for adjusting the tunnel flows that are required at each step of the overall adaptive-wall iterative process.[3,4]

These adjustment procedures would provide the logic for the ultimate automation of adaptive-wall wind tunnels. A first step toward logical procedures for tunnel adjustment is described in the next section.

IV. Influence Functions Due to Plenum-Pressure Change

As a first step toward development of automated wall-adjustment procedures, a study was made of the effect on the flow produced by changing the pressure p_n in one plenum chamber at a time while holding the pressure in the other chambers constant. The example described in Sec. III was chosen for these calculations. Numerous cases were investigated, including plenum chambers at various streamwise locations in the tunnel with suction and with blowing.

In one pair of examples, the pressure in plenum 6 (see Fig. 1) was changed by amounts such that $v_w(x_6)/U_\infty$ was changed by ± 0.0100 (and so c_{p6} by -0.031 and 0.053, respectively), where x_n is the x coordinate of the center of plenum n. The overall changes in $v_w(x)$ over plenum 6 are shown in Fig. 3. The $v_e(x)$ distributions that result from the boundary-layer calculation are shown in Fig. 4. It is remarkable that these resulting $v_e(x)$ distributions are changed significantly along the length of that plenum chamber, but negligibly at all other chambers, even those immediately downstream. This behavior occurs for all examples considered, whether the basic condition is suction or blowing at the plenum chamber where the pressure change is made. This does not imply that the boundary layer is unaffected downstream. Many of its properties, e.g., δ^* and θ, change appreciably downstream; however, $d(U_e\delta^*)/dx$ and hence $v_e(x)$ from Eq. (4) are not affected significantly there.

Results from the inviscid-flow calculation for the increased-suction example of Fig. 4 ($\Delta v_w(x_6)/U_\infty = -0.0100$ or $\Delta c_{p6} = 0.053$) are shown as the circles in Figs. 5 and 6. When the circles are compared with the baseline simulation represented by the crosses, it is observed in Fig. 5 that u has increased upstream and decreased downstream of plenum 6 at both control surfaces, with a crossover at plenum 6 itself. This behavior is consistent with the presence of a sink at the wall of a confined channel, such as exists here. An increase in suction (or a decrease in blowing) at one plenum chamber gives rise to an increased sink strength at that wall location. Conversely, other results not presented here show that a decrease in suction (or an increase in blowing) gives rise to an increased source strength and the differences in the u distributions will be of opposite sign. This source (or sink) effect in an otherwise confined channel is felt even to large distances upstream and downstream, as observed in Fig. 5.

The sink effect described here was observed in an experiment performed in the Calspan One-Foot Adaptive-Wall Tunnel before this analysis was undertaken. The suction was increased simultaneously at both plenum chambers 5 and 15. The increased suction increased the flow velocity at that station far upstream where M_∞ is measured and set. In order to maintain the desired M_∞, compensating adjustments were made in the tunnel drive, effectively removing the upstream perturbation. Therefore, during experimental iterations at a constant M_∞, one can expect the primary changes in u to occur at and downstream of the plenum being adjusted.

On the other hand, the changes in the v distributions at the control surfaces, as shown in Fig. 6, occur only locally in the immediate vicinity of the plenum chamber at which the control is changed. There is only a slight effect at the same streamwise position on the opposite control surface and negligible effect upstream and downstream at both control surfaces. This localized behavior also was observed in the One-Foot Tunnel experiments.

The results of all the calculations in which the pressure in a single plenum chamber was changed while the remainder were held at their original pressures were analyzed and cast in terms of influence functions. The notation $\Delta u(x)$ will refer to the

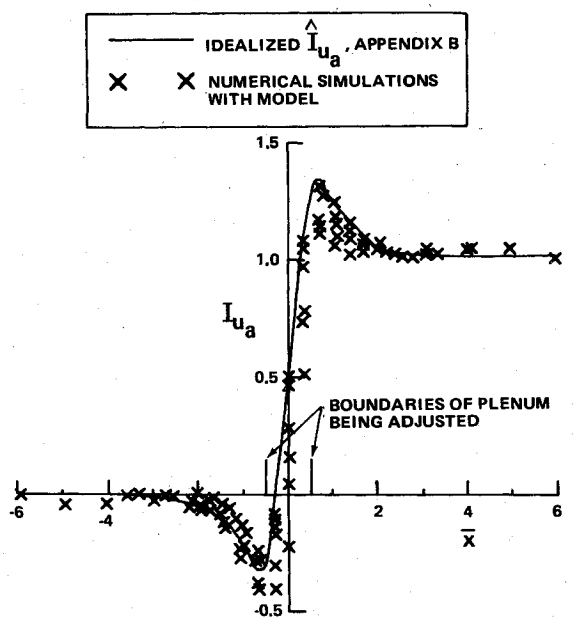

Fig. 8 Influence functions for streamwise velocity component at control surface adjacent to plenum being adjusted.

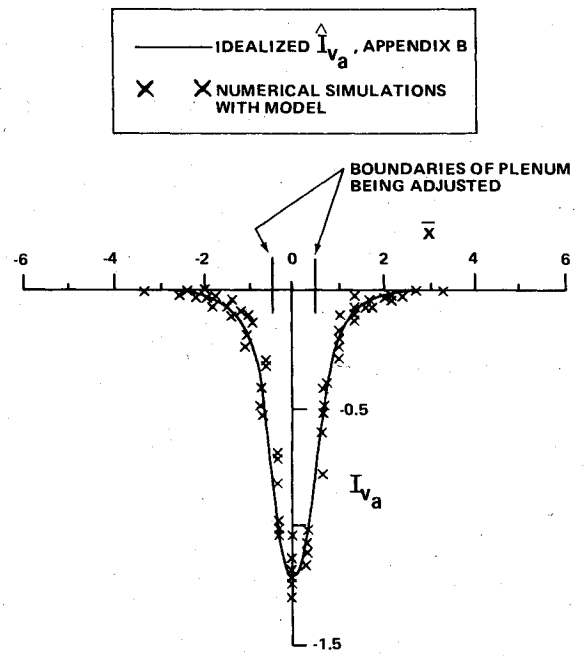

Fig. 9 Influence functions for normal velocity component at control surface adjacent to plenum being adjusted.

difference given by the streamwise velocity perturbation after a plenum adjustment has been made minus its value in the baseline simulation; an analogous definition is made for $\Delta v(x)$. If $\delta u \equiv \Delta u(\infty) - \Delta u(-\infty)$ is the difference in this calculated perturbation over the length of the test section, then a natural form for expressing the influence functions is

$$I_u(\bar{x}) = [\Delta u(\bar{x}) - \Delta u(-\infty)]/\delta u \tag{5}$$

$$I_v(\bar{x}) = -|\Delta v(\bar{x})/\delta u| \tag{6}$$

where $\bar{x} = (x - x_n)/\ell_n$ is a coordinate normalized by ℓ_n, the length of plenum n. The normalization in Eqs. (5) and (6) reflects the experimental situation in which the tunnel operator removes any Δu that is introduced far upstream so as

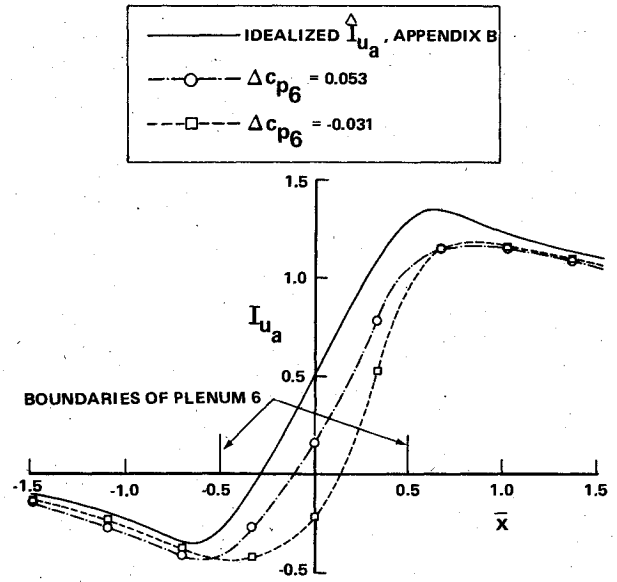

Fig. 10 Amplified distributions of influence functions for streamwise velocity component at control surface adjacent to plenum 6.

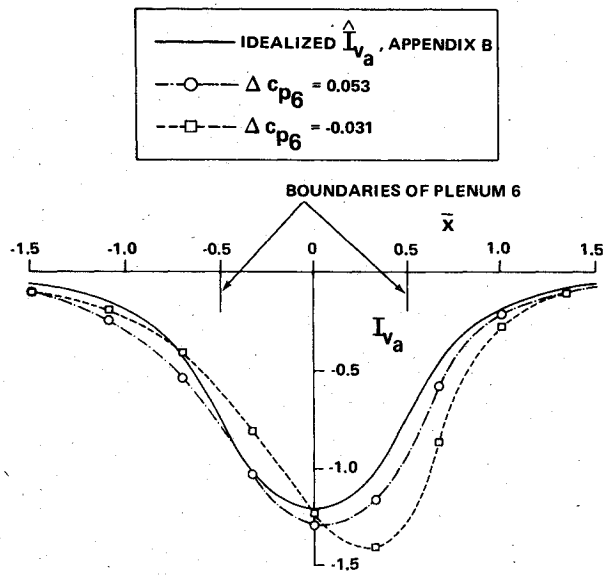

Fig. 11 Amplified distributions of influence functions for normal velocity component at control surface adjacent to plenum 6.

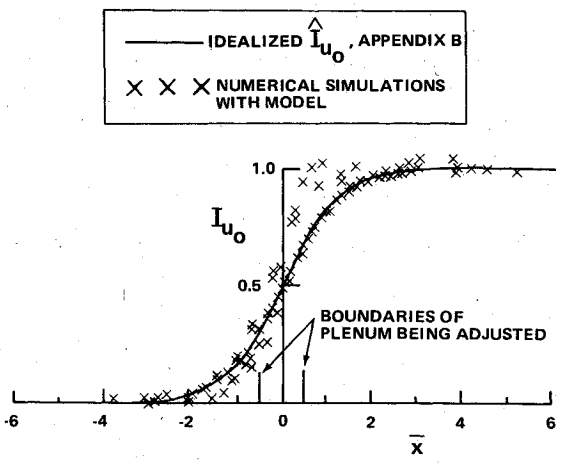

Fig. 12 Influence functions for streamwise velocity component at control surface opposite to plenum being adjusted.

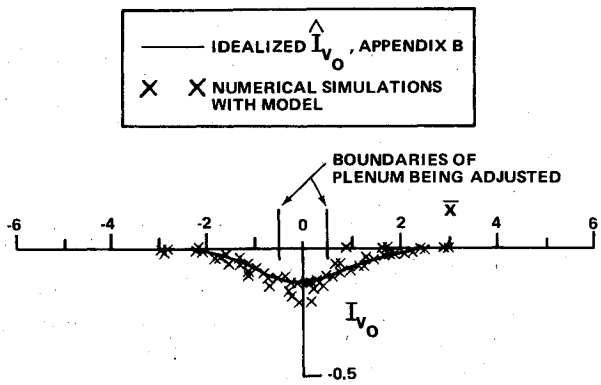

Fig. 13 Influence functions for normal velocity component at control surface opposite to plenum being adjusted.

to maintain a constant M_∞; hence $I_u(-\infty)=0$ and $I_u(\infty)=1$.

The influence functions I_{u_a} and I_{v_a}, where the subscript a denotes the control surface adjacent to plenum n, are presented in Figs. 8 to 11 as functions of $\bar{x}$, where the lines at $\bar{x}=\pm 0.5$ demarcate the ends of plenum n. In Figs. 8 and 9, the data from all the plenum chambers considered in the calculations are plotted, namely, plenum chambers 2, 3, and 6 with increased suction, plenum 6 with decreased suction, and plenum chambers 11, 13, and 16 with increased blowing. For comparison, idealized influence functions $\hat{I}_{u_a}$ and $\hat{I}_{v_a}$ are plotted as solid curves. These idealizations are derived in Appendix B using linearized theory without a model present, and assume a uniform $\Delta v_e(\bar{x})$ between $\bar{x}=\pm 0.5$. Figures 10 and 11 are plotted to an enlarged $\bar{x}$ scale to illustrate how the details of the changes in the v_e distribution in Fig. 4 affect the influence functions in the immediate vicinity of plenum 6. Since the increments in v_e in that vicinity are larger at the downstream end of the plenum than at the upstream end, I_{u_a} and I_{v_a} in Figs. 10 and 11 are skewed as shown. Farther away from the plenum the idealized influence functions, which assume a constant Δv_e along the plenum, provide a satisfactory approach to the asymptotic conditions.

The influence functions I_{u_o} and I_{v_o}, where the subscript o denotes the control surface at the opposite side of the tunnel from plenum n, are presented in Figs. 12 and 13. Again the details of the boundary-layer behavior at plenum n primarily affect the distribution only in the immediate vicinity of that plenum, whereas behavior away from this region is approximated reasonably well by the idealized representations $\hat{I}_{u_o}$ and $\hat{I}_{v_o}$.

The fact that the idealized distributions $\hat{I}_u$ and $\hat{I}_v$ derived for linearized, empty-tunnel flows are such a good representation of the distributions computed with the model present, I_u and I_v, is quite remarkable. As can be seen from the derivation of the linearized model, the general behavior is a function only of plenum length and the distance of the control surfaces from the walls. It is expected that other segmented-plenum configurations, e.g., those with slotted walls or those with perforated walls of different open-area ratios or slanted holes, should exhibit the same general characteristics.

The relationship between the change in pressure Δp_n, say, in plenum n and the total change in the u component, δu, will depend on the wall geometry, of course. This relationship depends on the details of the boundary layer and the wall characteristics. For the Calspan One-Foot Tunnel walls the relationship is implicitly represented by the form of Eqs. (1-4). For example, in the cases presented in Figs. 3 and 4, the increment $\Delta c_{p_6}=-0.0310$ results in $\delta u/U_\infty=0.0069$ and the increment $\Delta c_{p_6}=0.0530$ results in $\delta u/U_\infty=-0.0037$, where

these cases represent increments in $\Delta v_w(x_6)/U_\infty$ of 0.0100 and −0.0100, respectively.

There are two important next steps in development of this simulation and influence-function technique. The first would be extension of the analysis to compressible flows. As mentioned in Sec. III, no significant differences are expected until supercritical-flow conditions are reached. Then it is expected that I_u and I_v would depart significantly from idealized subsonic behavior. The other step would be experimental verification of influence-function behavior by measurement of the appropriate quantities. This would be straightforward but was beyond the scope of the experimental programs performed thus far. Bodapati et al.[14] have measured I_{v_a} and I_{v_o} for empty-tunnel conditions in their segmented-plenum, slotted-wall test section. Their results are generally of the form predicted here.

Once the validity of the predicted influence-function behavior has been established explicitly, the techniques can be used to investigate automated control procedures. In the Calspan experiments, the u component is set along the control surfaces so that I_{u_a} and I_{u_o} are of principal importance. In order to effect a change in u at each control point, one must find the sum of the changes induced at that point due to pressure changes Δc_{p_n} in each of the n plenum chambers. Since similar changes are desired at all the control points, a system of equations can be derived relating the prescribed changes in u to the plenum-pressure changes. This system of equations must be solved for the Δc_{p_n} that are necessary to achieve the desired flow. Since the influence functions of Eqs. (5) and (6) are defined in terms of δu, this quantity must be related to the pressure change Δc_{p_n} for each plenum. As discussed, this relationship is a highly nonlinear one. Use of both the idealized and the more exact relationships could be investigated by simulations to establish the accuracy to which the influence functions must be represented in the vicinity of each control plenum to iterate automatically and quickly to unconfined flow.

V. Concluding Remarks

The following are viewed as the principal results and conclusions drawn from the present investigation. To the authors' knowledge, the baseline simulation represents the first realistic numerical demonstration that an adaptive-wall wind tunnel with imperfect wall control can nevertheless achieve what is, for most practical purposes, unconfined flow about the model (see Fig. 7). This was accomplished in spite of the fact that the modeling of the wall transpiration characteristics and boundary layers was relatively crude and, if anything, exacerbated the effects of imperfect control.

Assuming that the tunnel drive is trimmed to keep the freestream conditions constant, the major influence of an adjustment in plenum pressure on the streamwise velocity component will be felt at and downstream of the plenum being adjusted (Figs. 8 and 12). The major influence of a change in plenum pressure on the normal velocity component is much more localized, being significant only in the immediate vicinity of the plenum being adjusted (Figs. 9 and 13).

When suitably normalized [Eqs. (5) and (6)], the influence functions describing the above behavior fall on a more or less universal curve whose shape is likely to be independent of the particular wall geometry studied here. In fact, its shape is predicted quite well by an idealized, linear theory (Appendix B) at positions away from the adjusted plenum. However, changes in both velocity components in the immediate vicinity of the plenum being adjusted are influenced by the details of the distribution of suction/blowing over that plenum (Figs. 10 and 11).

The relationship between the normalization factor δu used in Eqs. (5) and (6) and the plenum pressure is essentially determined by the wall characteristics, which in turn will depend on the particular wall geometry used.

For those plenum chambers where suction is applied, control of the inviscid flow can be expected to be linear or nearly so. When blowing is used, however, the flow is likely to respond in a nonlinear manner to plenum adjustments (Appendix A).

Although the present simulations are confined to low-speed flow for simplicity, the extension to compressible subsonic speeds is not expected to alter these conclusions qualitatively, provided the flow remains subcritical. For supercritical wall conditions, which may prove of great practical significance, a model of shock-wave/boundary-layer interaction would have to be added; the attendant possibility of separated flow at the wall and the sensitivity of shock-wave position to details of the flow at the walls may lead to qualitatively new phenomena. Once this question is answered, application of the model to simulating the actual iterative wall-control process[3,4] at high subsonic speeds should be possible.

Appendix A—Boundary-Layer Model and Amplification Effect

For the purpose of studying the effects of the boundary layer on the inviscid interior flow, it is the integral properties of the layer, as opposed to the detailed profiles across it, that are of primary interest. Accordingly, an integral (as opposed to finite-difference) method was chosen as the most efficient means to model the boundary layer. The particular method used is that first proposed by Head,[30] which had been applied successfully by others in predicting the behavior of transpired turbulent layers.[31,32]

Basically Head's method consists of simultaneously solving three equations. The first is his so-called entrainment equation,

$$\frac{1}{U_e}\frac{\mathrm{d}}{\mathrm{d}x}(U_e\theta H_1) = F(H_1) + \frac{v_w}{U_e} \tag{A1}$$

where H_1 is a modified shape factor defined by $H_1 \equiv (\delta - \delta^*)/\theta$, and U_e is the local streamwise velocity at the layer's edge. Here δ, δ^*, and θ refer, respectively, to the boundary-layer, displacement, and momentum thicknesses. H_1 is related to the more conventional shape factor $H \equiv \delta^*/\theta$ by $H_1 = G(H)$. The functions $F(H_1)$ and $G(H)$ were derived empirically from existing data. The rationale behind Eq. (A1) can be found in Refs. 30-32.

The second equation is

$$\frac{\mathrm{d}\theta}{\mathrm{d}x} + \frac{\theta}{U_e}(H+2)\frac{\mathrm{d}U_e}{\mathrm{d}x} - \frac{v_w}{U_e} = \frac{c_f}{2} \tag{A2}$$

which is simply the well-known von Kármán integral momentum equation derived in most boundary-layer texts. The only new quantity introduced is c_f, the local skin-friction coefficient.

Head's original applications were to solid-wall boundary layers for which he used the Ludwieg-Tillmann correlation[33] to predict c_f. For the present application this procedure was modified as follows: first, the Ludwieg-Tillmann correlation was used to compute c_{f_0}, the skin-friction coefficient that would obtain if no transpiration were present,

$$c_{f_0} = (0.246)\,10^{-0.678H} Re_\theta^{-0.268} \tag{A3}$$

where Re_θ is the local momentum-thickness Reynolds number. This value was then corrected for the effects of blowing or suction via the empirical correction suggested by Simpson, Moffat, and Kays[34]:

$$\frac{c_f}{c_{f_0}} = \left[\frac{\ln|1+B|}{B}\right]^{0.7} \tag{A4}$$

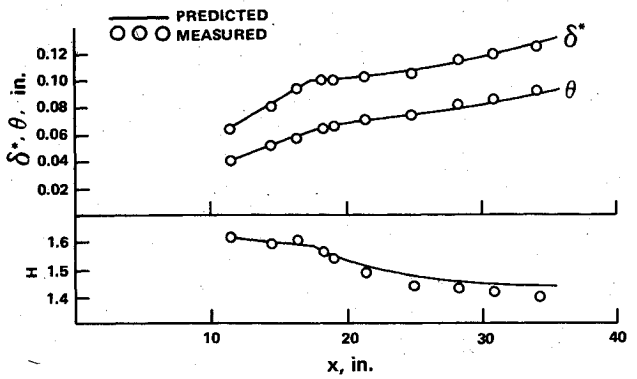

Fig. A1 Comparison of predicted and measured boundary-layer characteristics (discontinuous blowing experiment of McQuaid,[32] $v_w/U_\infty = 0.0035$ for $x < 17.5$ in., $v_w/U_\infty = 0$ for $x > 17.5$ in.).

where $B = 2v_w/c_f U_e$. Because of the implicit dependence of B on c_f and the transcendental nature of Eq. (A4), it had to be solved using Newton-Raphson iteration, but the convergence is quite rapid.

The above system of three equations (two differential, one algebraic) was solved for the three unknowns θ, H, and c_f using a Runge-Kutta procedure. Required inputs are the distributions $U_e(x)$ and $v_w(x)$ and initial conditions on θ and H at the starting point.

To validate the boundary-layer program, its predictions were compared with experimental data of other investigators for several representative flows, including various streamwise pressure gradients with and without transpiration. An example of particular interest to the present application is an experimental configuration investigated by McQuaid.[32] In this case, there was uniform blowing of constant strength up to $x^* = 0.444$ m (17.5 in.); downstream of this point v_w was nominally zero. The equations were integrated up to x^* using the experimental values of θ and H at $x = 0.292$ m (11.5 in.) as initial conditions and $v_w/U_\infty = 0.0035$. The calculated values of θ and H at x^* were then used as initial conditions for further integration downstream with $v_w/U_\infty = 0$. Results of the calculation are compared with McQuaid's data in Fig. A1; English units have been used, as this was the form in which the data were first published.[32] The predicted development of δ^*, θ, and H from their initial values agrees well with the data. In particular, the calculated distributions display discontinuities in their slopes at the discontinuity in blowing velocity, and this behavior reflects the observed variation there reasonably well. This and other comparisons gave confidence in the ability of the model to predict adequately the integral properties of the boundary layer.

The first application of the boundary-layer model specifically to the Calspan One-Foot Tunnel configuration shown in Fig. 1 was done to see whether it confirmed a so-called boundary-layer-amplification effect that had been noted in adjusting the plena to achieve a desired flow condition. In early experiments with the model present in the tunnel,[4] it was observed in many cases that the normal velocity measured by a probe 0.038 m (1.5 in.) from the wall was considerably greater in magnitude than v_w, the velocity at the wall itself. Although part of this amplification was due to the increase over that distance in the inviscid velocity induced by the model, there was still a marked increase in magnitude of the amplification as more blowing was applied. Accordingly, the present boundary-layer computational method was used to examine the relationship between v_e and v_w, i.e., to cast light on the amplification of the normal velocity across the boundary layer. For these calculations, flow without the model present was represented by assuming uniform flow over a flat surface with zero streamwise pressure gradient. With the assumption of constant transpiration velocity along the controlled section, calculations were made to cover the range $-0.0275 \le v_w/U_\infty \le 0.0150$. A plot of v_e/U_∞ vs v_w/U_∞

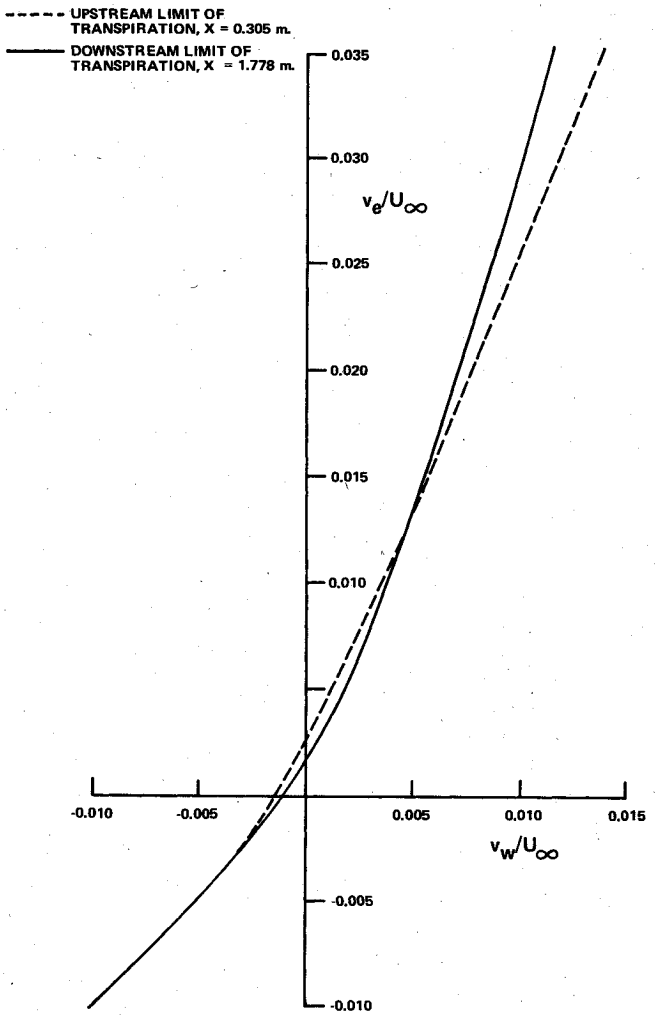

Fig. A2 Calculated inviscid normal velocity v_e/U_∞ due to boundary-layer displacement on flat wall with transpiration velocity v_w/U_∞ and zero pressure gradient.

over part of this range is given in Fig. A2 for locations corresponding to the upstream and downstream limits of the controlled test section length and shows only a weak dependence on x. When $v_w/U_\infty < -0.0050$, there appears to be an asymptotic suction behavior of the same nature that exists in laminar flow.[35] That is, the boundary layer ceases to grow, and its integral properties, particularly δ^*, become independent of x. Equation (4) then predicts that $v_e = v_w$, so that the slope of the curve in this region is just unity and there is no amplification by the boundary layer. As v_w/U_∞ increases above -0.0050, however, the slope of the curve in Fig. A2 increases significantly, and in the region of blowing, v_e greatly exceeds v_w. Not only has the first term on the right-hand side of Eq. (4) increased, but this increase in turn has greatly magnified the boundary-layer growth represented by the second term; since these terms are additive, amplification of the normal velocity across the layer results. Jacocks[36] has performed calculations with a finite-difference boundary-layer code and experimentally determined wall-pressure data with a model present. The envelope he determined for his calculated results is quite similar to that exhibited in Fig. A2.‡

In addition to helping in an understanding of the simulation results discussed in the main text, Fig. A2 carries a very practical lesson for the users of such adaptive-wall tunnels; namely, control of inviscid flow via plenum adjustments is linear and well behaved for suction, but likely to be highly nonlinear when blowing is needed.

‡Subsequent to acceptance of the present manuscript, the authors' attention was drawn to Ref. 40, which contains additional experimental and numerical support for these conclusions.

Appendix B—Idealized Influence Functions

In this appendix, an idealized form of the influence functions of Sec. IV is found. A linear approximation for the flow in a tunnel without the model present has been chosen. Thus, the idealized analysis here will be related to the differences found in the results of the simulations of Sec. IV when the pressure is changed in one plenum while the pressure is held constant in the other chambers. These relationships will be pointed out as the analysis proceeds.

The ξ, η coordinate system used here is the same as the x, y system in Fig. 1 except that the origin of ξ is located in line with the center of the plenum chamber being adjusted, which has length ℓ_n, whereas the origin of x is at the quarter chord of the model. In the ξ, η system, the flow investigated is induced by a uniform normal velocity v_I imposed at the upper wall over the interval $-\ell_n/2 \le \xi \le \ell_n/2$ with $v=0$ prescribed everywhere else on the upper wall as well as on the entire lower wall. The freestream velocity is U_∞ and the streamwise disturbances u are assumed to be zero far upstream, just as in the experiments. The magnitude of v_I is related to the differences in the integral of $v_e(x)$ over the length of plenum n as carried out before and after the pressure in that plenum is changed.

The linearized compressible-flow analysis is carried out in the Prandtl-Glauert approximation, so that a disturbance velocity potential ϕ exists and satisfies

$$\beta^2 \phi_{\xi\xi}(\xi,\eta) + \phi_{\eta\eta}(\xi,\eta) = 0 \tag{B1}$$

where $\beta^2 = 1 - M_\infty^2$ and the subscripts ξ and η denote partial differentiation with respect to those variables. The boundary conditions that the u disturbance-velocity component must be zero at infinity upstream and that v at the walls must be as described above are expressed as

$$\phi_\xi(-\infty,\eta) = 0 \tag{B2}$$

$$\phi_\eta(\xi,-h) = 0 \tag{B3}$$

$$\phi_\eta(\xi,h) = \begin{cases} v_I, & -\ell_n/2 < \xi < \ell_n/2 \\ 0, & |\xi| > \ell_n/2 \end{cases} \tag{B4}$$

The problem is solved by means of Fourier transforms, which are defined as

$$\bar{\phi}(\eta;s) = \frac{1}{\sqrt{2\pi}} \int_{-\infty}^{\infty} \phi(\xi,\eta) e^{is\xi} d\xi \tag{B5}$$

$$\phi(\xi,\eta) = \frac{1}{\sqrt{2\pi}} \int_{-\infty}^{\infty} \bar{\phi}(\eta;s) e^{-is\xi} ds \tag{B6}$$

Upon transformation, Eq. (B1) becomes

$$-\beta^2 s^2 \bar{\phi}(\eta;s) + \bar{\phi}_{\eta\eta}(\eta;s) = 0 \tag{B7}$$

which is an ordinary differential equation with the solution

$$\bar{\phi}(\eta;s) = A_1 e^{\beta s\eta} + A_2 e^{-\beta s\eta} + A_3 \tag{B8}$$

where A_1 to A_3 are constants. Since the constant A_3 transforms back to the ξ, η coordinates as a delta function, which has no physical significance in this problem, A_3 is taken to be zero. The boundary condition of Eq. (B2) will be satisfied later after transformation back to the ξ coordinate. The boundary conditions of Eqs. (B3) and (B4) transform to

$$\bar{\phi}_\eta(-h;s) = 0 \tag{B9}$$

$$\bar{\phi}_\eta(h;s) = 2v_I \sin(s\ell_n/2)/\sqrt{2\pi s} \tag{B10}$$

Performing the appropriate operations on Eqs. (B8-B10) yields

$$\bar{\phi}(\eta;s) = \frac{2v_I \sin(s\ell_n/2)\cosh[\beta s(\eta+h)]}{\sqrt{2\pi}\beta s^2 \sinh(2\beta sh)} \tag{B11}$$

The potential itself is then found by substitution in Eq. (B6). Since the right-hand side of Eq. (B11) is an even function of s, this result can be simplified to

$$\phi(\xi,\eta) = \frac{2v_I}{\pi\beta} \times \int_0^\infty \frac{\cosh[\beta(\eta+h)s]\operatorname{csch}(2\beta hs)\sin(\ell_n s/2)\cos\xi s}{s^2} ds \tag{B12}$$

Differentiating this twice with respect to ξ gives

$$\phi_{\xi\xi}(\xi,\eta) = -\frac{v_I}{\pi\beta} \int_0^\infty \cosh[\beta(\eta+h)s]\operatorname{csch}(2\beta hs) \times \{\sin[(\xi+\ell_n/2)s] - \sin[(\xi-\ell_n/2)s]\} ds \tag{B13}$$

which can be integrated[37] to give

$$\phi_{\xi\xi}(\xi,\eta) = -\frac{v_I}{4\beta^2 h} \left\{ \frac{\sinh\left[\frac{\pi(\xi+\ell_n/2)}{2\beta h}\right]}{\cosh\left[\frac{\pi(\xi+\ell_n/2)}{2\beta h}\right] + \cos\left[\frac{\pi(\eta+h)}{2h}\right]} - \frac{\sinh\left[\frac{\pi(\xi-\ell_n/2)}{2\beta h}\right]}{\cosh\left[\frac{\pi(\xi-\ell_n/2)}{2\beta h}\right] + \cos\left[\frac{\pi(\eta+h)}{2h}\right]} \right\} \tag{B14}$$

The u component is found by integrating Eq. (B14) with respect to ξ. The constant of integration is chosen so as to satisfy Eq. (B2), and the result is

$$\phi_\xi(\xi,\eta) = -\frac{v_I \ell_n}{2\beta^2 h} \times \left[\frac{1}{2} + \frac{\beta h}{\pi \ell_n} \ln \left\{ \frac{\cosh\left[\frac{\pi(\xi+\ell_n/2)}{2\beta h}\right] + \cos\left[\frac{\pi(\eta+h)}{2h}\right]}{\cosh\left[\frac{\pi(\xi-\ell_n/2)}{2\beta h}\right] + \cos\left[\frac{\pi(\eta+h)}{2h}\right]} \right\} \right] \tag{B15}$$

The desired v component is found in a similar fashion. Using Eq. (B14) in conjunction with Eq. (B1) gives an equation for $\phi_{\eta\eta}(\xi,\eta)$ that can be integrated with respect to η to yield

$$\phi_\eta(\xi,\eta) = \frac{v_I}{\pi} \left[\operatorname{sgn}(\xi+\ell_n/2)\tan^{-1}\left\{ \tanh\left[\frac{\pi|\xi+\ell_n/2|}{4\beta h}\right] \times \tan\left[\frac{\pi(\eta+h)}{4h}\right] \right\} - \operatorname{sgn}(\xi-\ell_n/2) \times \tan^{-1}\left\{ \tanh\left[\frac{\pi|\xi-\ell_n/2|}{4\beta h}\right] \tan\left[\frac{\pi(\eta+h)}{4h}\right] \right\} \right] \tag{B16}$$

where the constant of integration is zero by Eq. (B3) and $\operatorname{sgn}(\xi)$ is ± 1 according to whether $\xi \gtrless 0$.

The results are now cast in terms of the variables $\bar{x}$ and $\bar{y}$, where $\bar{x}=\xi/\ell_n$ and $\bar{y}=\eta/h$. In particular, the idealized influence functions, denoted by $\hat{I}_u$ and $\hat{I}_v$ to distinguish them from those calculated in the simulations, are found from Eqs. (B15) and (B16). From Eq. (B15), it follows that $\phi_\xi(-\infty,\eta)=0$ and $\phi_\xi(\infty,\eta)=-v_1\ell_n/2h\beta^2$, so that in terms of Eqs. (5) and (6), $\delta u=\phi_\xi(\infty,\eta)-\phi_\xi(-\infty,\eta)=-v_1\ell_n/2h\beta^2$. Thus both ϕ_ξ and ϕ_η must be divided by this factor to get $\hat{I}_u$ and $\hat{I}_v$, which for incompressible flow ($\beta=1$) are

$$\hat{I}_u(\bar{x},\bar{y})=\frac{1}{2}+\frac{h}{\pi\ell_n}\times\ell n\left\{\frac{\cosh\left[\frac{\pi\ell_n(\bar{x}+\frac{1}{2})}{2h}\right]+\cos\left[\frac{\pi(\bar{y}+1)}{2}\right]}{\cosh\left[\frac{\pi\ell_n(\bar{x}-\frac{1}{2})}{2h}\right]+\cos\left[\frac{\pi(\bar{y}+1)}{2}\right]}\right\} \tag{B17}$$

$$\hat{I}_v(\bar{x},\bar{y})=-\frac{2h}{\pi\ell_n}\left[\operatorname{sgn}(\bar{x}+\tfrac{1}{2})\times\tan^{-1}\left\{\tanh\left[\frac{\pi\ell_n|\bar{x}+\frac{1}{2}|}{4h}\right]\tan\left[\frac{\pi(\bar{y}+1)}{4}\right]\right\}-\operatorname{sgn}(\bar{x}-\tfrac{1}{2})\times\tan^{-1}\left\{\tanh\left[\frac{\pi\ell_n|\bar{x}-\frac{1}{2}|}{4h}\right]\tan\left[\frac{\pi(\bar{y}+1)}{4}\right]\right\}\right] \tag{B18}$$

The $\hat{I}_{u_a}$, $\hat{I}_{v_a}$, $\hat{I}_{u_o}$, and $\hat{I}_{v_o}$ curves of Figs. 8 to 13 were evaluated from Eqs. (B17) and (B18) for $\ell_n/h=1$ and $\bar{y}=y_c/h=\pm0.655$. The expression for $\hat{I}_u(\bar{x},\bar{y})$ in Eq. (B17) is valid everywhere except at the two points $\bar{y}=1$, $\bar{x}=\pm\frac{1}{2}$, where there are singularities introduced by the discontinuities in v at these points. As is well known in linearized thin-airfoil theory, such a discontinuity leads to a logarithmic singularity in u there. (See Refs. 38 and 39 for the singularity at the kink in a bent flat plate.) In the calculated values of $\hat{I}_u$ shown in Figs. 8 and 10, there are no singularities because $\bar{y}=\pm0.655$, but the overshoot observed near $\bar{x}=\pm\frac{1}{2}$ has its origin in that singular behavior.

Acknowledgments

This investigation was sponsored jointly by the Office of Naval Research and the Air Force Office of Scientific Research. The authors wish to thank the technical monitors, Mr. M. Cooper of ONR and Dr. J. D. Wilson of AFOSR, as well as their Calspan colleagues Dr. J. P. Nenni and Mr. C. E. Wittliff and Calspan consultant Prof. W. R. Sears of the University of Arizona for their useful discussions of this research.

References

[1] Ferri, A. and Baronti, P., "A Method for Transonic Wind Tunnel Corrections," *AIAA Journal*, Vol. 11, Jan. 1973, pp. 63-66.

[2] Sears, W. R., "Self-Correcting Wind Tunnels," (The Sixteenth Lanchester Memorial Lecture), *Aeronautical Journal*, Vol. 78, Feb./March 1974, pp. 80-89.

[3] Sears, W. R., Vidal, R. J., Erickson, J. C., Jr., and Ritter, A., "Interference-Free Wind-Tunnel Flows by Adaptive-Wall Technology," ICAS Paper No. 76-02, Oct. 1976; see also *Journal of Aircraft*, Vol. 14, Nov. 1977, pp. 1042-1050.

[4] Vidal, R. J., Erickson, J. C., Jr., and Catlin, P. A., "Experiments with a Self-Correcting Wind Tunnel," AGARD-CP-174, Oct. 1975.

[5] Vidal, R. J. and Erickson, J. C. Jr., "Experiments on Supercritical Flows in a Self-Correcting Wind Tunnel," AIAA Paper 78-788, April 1978.

[6] Vidal, R. J. and Erickson, J. C. Jr., "Research on Adaptive Wall Wind Tunnels," AEDC TR 78-36, Nov. 1978.

[7] Erickson, J. C. Jr., Wittliff, C. E., and Daughtry, D. C., "Further Investigations of Adaptive-Wall Wind Tunnels," AEDC TR 80-34, Oct. 1980.

[8] Erickson, J. C. Jr., Wittliff, C. E., and Padova, C., "Adaptive-Wall Wind-Tunnel Experiments with Supercritical Flow at the Walls," Calspan Corp., Buffalo, N.Y., RK-6040-A-2, Feb. 1981.

[9] Chevallier, J. P., "Soufflerie Transonique a Parois-Adaptables," AGARD-CP-174, Oct. 1975; also translated into English as European Space Agency Rept. ESA-TT-326, Oct. 1976, available as NASA Accession No. N77-13085.

[10] Goodyer, M. J. and Wolf, S.W.D., "Development of a Self-Streamlining Flexible Walled Transonic Test Section," *AIAA Journal*, Vol 20, Feb. 1982, pp. 227-234.

[11] Ganzer, U., "Adaptable Wind Tunnel Walls for 2-D and 3-D Model Tests," ICAS Paper 23.3, Oct. 1980.

[12] Kraft, E. M. and Parker, R. L. Jr., "Experiments for the Reduction of Wind Tunnel Wall Interference by Adaptive-Wall Technology," AEDC TR 79-51, Oct. 1979.

[13] Parker, R. L. Jr., and Sickles, W. L., "Application of Adaptive Wall Techniques in a Three-Dimensional Wind Tunnel with Variable Wall Porosity," *Journal of Aircraft*, Vol. 18, March 1981, pp. 176-183.

[14] Bodapati, S., Schairer, E., and Davis, S., "Adaptive-Wall Wind-Tunnel Development for Transonic Testing," *Journal of Aircraft*, Vol. 18, April 1981, pp. 273-279.

[15] Erickson, J. C. Jr. and Nenni, J. P., "A Numerical Demonstration of the Establishment of Unconfined-Flow Conditions in a Self-Correcting Wind Tunnel," Calspan Corp., Buffalo, N. Y., RK-5070-A-1, Nov. 1973.

[16] Sears, W. R., "A Note on Adaptive-Wall Wind Tunnels," *Zeitschrift fur angewandte Mathematik und Physik*, Vol. 28, 1977, pp. 915-927.

[17] Lo, C. F. and Kraft, E. M., "Convergence of the Adaptive-Wall Wind Tunnel," *AIAA Journal*, Vol. 16, Jan. 1978, pp. 67-72.

[18] Lo, C. F. and Sickles, W. L., "Analytical and Numerical Investigation of the Convergence of the Adaptive-Wall Concept," AEDC TR 79-55, Nov. 1979.

[19] Sears, W. R., "Adaptive Wind Tunnels with Imperfect Control," *Journal of Aircraft*, Vol. 16, May 1979, pp. 344-348.

[20] Brady, W. G. and Ludwig, G. R., "Theoretical and Experimental Investigation of the Aerodynamic Properties of Airfoils Near Stall in Two-Dimensional Nonuniformly Sheared Flow," U.S. Army AVLABS TR 66-36, June 1966.

[21] Ludwig, G. R. and Erickson, J. C. Jr., "Airfoils in Two-Dimensional Nonuniformly Sheared Slipstreams," *Journal of Aircraft*, Vol. 8, Nov. 1971, pp. 874-880.

[22] von Mises, R., *Theory of Flight*, McGraw-Hill, New York, 1945, pp. 188-198.

[23] Phillips, B. L., "A Technique for the Numerical Solution of Certain Integral Equations of the First Kind," *Journal of the Association for Computing Machinery*, Vol. 9, Jan. 1962, pp. 84-97.

[24] Twomey, S., "On the Numerical Solution of Fredholm Integral Equations of the First Kind by the Inversion of the Linear System by Quadrature," *Journal of the Association for Computing Machinery*, Vol. 10, Jan. 1963, pp. 97-101.

[25] Chew, W. L., "Cross-Flow Calibration at Transonic Speeds of Fourteen Perforated Plates with Round Holes and Airflow Parallel to the Plates," AEDC TR 54-65, July 1955.

[26] Goethert, B. H., *Transonic Wind Tunnel Testing*, Pergamon Press, New York, 1961, Chap. 11.

[27] Lighthill, M. J., "On Displacement Thickness," *Journal of Fluid Mechanics*, Vol. 4, Aug. 1958, pp. 383-392.

[28] Hess, J. L., "Review of Integral-Equation Techniques for Solving Potential-Flow Problems with Emphasis on the Surface Source Method," *Computer Methods in Applied Mechanics and Engineering*, Vol. 5, 1975, pp. 145-196.

[29] Melnik, R. E., "Wake Curvature and Trailing Edge Interaction Effects in Viscous Flow over Airfoils," NASA CP-2045, Part 1, Vol. I, March 1979, pp. 255-270.

[30] Head, M. R., "Entrainment in the Turbulent Boundary Layer," Aeronautical Research Council, R&M No. 3152, Sept. 1958.

[31] Thompson, B.G.J., "The Calculation of Shape-Factor Development in Incompressible Turbulent Boundary Layers with or Without Transpiration," *Recent Developments in Boundary Layer Research*, AGARDograph 97, May 1965, Pt. I.

[32] McQuaid, J., "The Calculation of Turbulent Boundary Layers with Injection," Aeronautical Research Council, R&M No. 3542, Jan. 1967.

[33] Ludwieg, H. and Tillmann, W., "Investigations of the Wall-Shearing Stress in Tubulent Boundary Layers," NACA TM 1285, May 1950.

[34] Simpson, R. L., Moffat, R. J., and Kays, W. M., "The Turbulent Boundary Layer on a Porous Plate: Experimental Skin Friction with Variable Injection and Suction," *International Journal of Heat and Mass Transfer*, Vol. 12, 1969, pp. 771-789.

[35] Schlichting, H., *Boundary Layer Theory*, McGraw-Hill, New York, 1955, pp. 229-236.

[36] Jacocks, J. L., "An Investigation of the Aerodynamic Characteristics of Ventilated Test Section Walls for Transonic Wind Tunnels," Ph.D. Thesis, University of Tennessee, Knoxville, Tenn., Dec. 1976 (University Microfilms No. 77-10777).

[37] Erdelyi, A., Magnus, W., Oberhettinger, F., and Tricomi, F. G., eds., *Tables of Integral Transforms*, Vol. 1, Bateman Manuscript Project, McGraw-Hill, New York, 1954, p. 88, Eq. 7.

[38] Glauert, H., "Theoretical Relationships for an Aerofoil with Hinged Flap," Aeronautical Research Council, R&M No. 1095, April 1927.

[39] Spence, D. A., "The Lift on a Thin Aerofoil with a Jet-Augmented Flap," *The Aeronautical Quarterly*, Vol. 9, Aug. 1958, pp. 287-299.

[40] Chan, Y. Y., "Analysis of Boundary Layers on Perforated Walls of Transonic Wind Tunnels," *Journal of Aircraft*, Vol. 18, June 1981, pp. 469-473.